A microtubule-dynein tethering complex regulates the axonemal inner dynein *f* (I1)

Tomohiro Kubo[a], Yuqing Hou[b], Deborah A. Cochran[b], George B. Witman[b], and Toshiyuki Oda[a,*]
[a]Department of Anatomy and Structural Biology, Graduate School of Medical Science, University of Yamanashi, 1110 Shimokato, Chuo, Yamanashi 409-3898, Japan; [b]Division of Cell Biology and Imaging, Department of Radiology, University of Massachusetts Medical School, Worcester, MA 01655

ABSTRACT **Motility of cilia/flagella is generated by a coordinated activity of thousands of dyneins. Inner dynein arms (IDAs) are particularly important for the formation of ciliary/flagellar waveforms, but the molecular mechanism of IDA regulation is poorly understood. Here we show using cryoelectron tomography and biochemical analyses of *Chlamydomonas* flagella that a conserved protein FAP44 forms a complex that tethers IDA *f* (I1 dynein) head domains to the A-tubule of the axonemal outer doublet microtubule. In wild-type flagella, IDA *f* showed little nucleotide-dependent movement except for a tilt in the *f*β head perpendicular to the microtubule-sliding direction. In the absence of the tether complex, however, addition of ATP and vanadate caused a large conformational change in the IDA *f* head domains, suggesting that the movement of IDA *f* is mechanically restricted by the tether complex. Motility defects in flagella missing the tether demonstrates the importance of the IDA *f*-tether interaction in the regulation of ciliary/flagellar beating.**

Monitoring Editor
Xueliang Zhu
Chinese Academy of Sciences

Received: Nov 30, 2017
Revised: Dec 29, 2017
Accepted: Jan 2, 2018

INTRODUCTION

Cilia and flagella are conserved organelles that generate fluid flow by their beating movement (Gibbons, 1981; Hirokawa *et al.*, 2006). In humans, defects in the assembly and motility of cilia and flagella result in multiple disorders (Pazour and Rosenbaum, 2002; Afzelius, 2004; Satir and Christensen, 2007). Ciliary beating is driven by the dynein motor proteins. The microtubule-sliding activity of dynein requires a series of conserved domains: the ring-shaped "head" consisting of six AAA ATPase units; a coiled-coil "stalk," which binds to the microtubule in an ATP-dependent manner; and the amino-terminal "tail," which works as a lever arm to generate the power stroke (King, 2000; Carter *et al.*, 2008; Cho and Vale, 2012; Kon *et al.*, 2012; Schmidt *et al.*, 2012). The axonemal dyneins are divided into two groups, the outer and the inner dynein arms (ODAs and IDAs). The ODAs and IDAs play distinct roles in ciliary movement; the ODAs produce forces for the control of beating frequency (Kamiya and Okamoto, 1985; Mitchell and Rosenbaum, 1985), while the IDAs determine the bend amplitude. There are seven (*a*–*g*) major and four minor subspecies of IDAs (Kagami and Kamiya, 1992; Bui *et al.*, 2012), but the functional differences among these IDA subspecies are poorly understood (Yagi *et al.*, 2005; Bui *et al.*, 2012; Kamiya and Yagi, 2014). IDA subspecies *f* (IDA *f*), also known as I1 dynein, is the only dimeric IDA and it is thought to be involved in the phototactic behavior of *Chlamydomonas* cells (King and Dutcher, 1997; Okita *et al.*, 2005). IDA *f* is also unique in that its two heavy chains (HCs), *f*α and *f*β, interact with a large intermediate chain–light chain (IC-LC) complex composed of three intermediate chains (IC140, IC138, and IC97), five light chains (LC7a, LC7b, LC8, Tctex1, and Tctex2b), and an accessory subunit FAP120 (Piperno *et al.*, 1990; Smith and Sale, 1991; Porter *et al.*, 1992; Myster *et al.*, 1997; Harrison *et al.*, 1998; Perrone *et al.*, 1998, 2000; Myster *et al.*, 1999; DiBella *et al.*, 2004a,b; Hendrickson *et al.*, 2004; Ikeda *et al.*, 2009; Toba *et al.*, 2011). Among these ICs and LCs, IC138 has been extensively studied (Habermacher and Sale, 1997; King and Dutcher, 1997; Yang *et al.*, 2000; Bower *et al.*, 2009; Wirschell *et al.*, 2009). Phosphorylation of IC138 by casein kinase1 or protein kinase A suppresses the microtubule sliding activity of axonemal dyneins, and dephosphorylation of IC138 by protein phosphatase 1 or 2A restores axonemal motility (Wirschell *et al.*, 2007; Gokhale *et al.*, 2009; Elam *et al.*, 2009). The

This article was published online ahead of print in MBoC in Press (http://www.molbiolcell.org/cgi/doi/10.1091/mbc.E17-11-0689) on January 29, 2018.
The authors have no competing financial interests to declare.
*Address correspondence to: Toshiyuki Oda (toda@yamanashi.ac.jp).
Abbreviations used: BCCP, biotin carboxyl carrier protein; FAP, flagellar associated protein; IC, intermediate chain; IDA, inner dynein arm; LC, light chain; MIA, modifier of inner arms; N-DRC, nexin-dynein regulatory complex; ODA, outer dynein arm; RS, radial spoke.

radial spoke is thought to be involved in this IC138-mediated regulation of the dynein activity because absence of the radial spoke induces hyperphosphorylation of IC138, and an A-kinase anchoring protein is localized at the base of the radial spoke (Gaillard *et al.*, 2001, 2006; Hendrickson *et al.*, 2004; VanderWaal *et al.*, 2011). In addition, the modifier of inner arms (MIA) structure, which bridges between the IC-LC complex and the nexin-dynein regulatory complex (N-DRC), suggests a functional communication between IC138 and the N-DRC (Yamamoto *et al.*, 2013). Despite these studies on the regulatory subunits, the poor in vitro microtubule-sliding activity of IDA *f* has precluded understanding of its mechanical properties and function in the axoneme (Smith and Sale, 1991; Kagami and Kamiya, 1992; Kotani *et al.*, 2007; Toba *et al.*, 2011). As the microtubule-sliding activity of IDA *c* is suppressed in the presence of IDA *f* in vitro, it has been proposed that IDA *f* acts as a drag on microtubule-sliding (Kotani *et al.*, 2007). A unique role for IDA *f* is also suggested by its appearance in the cryoelectron tomograms. The *f*α and *f*β heads are located closer to the A-tubule surface of the outer doublet microtubule (DMT) compared with other IDA heads, and the ring of the *f*α is tilted relative to the longitudinal axis of the DMT (Bui *et al.*, 2008). Moreover, the *f*α and *f*β heads appear to be anchored to the A-tubule via a large structure designated the "tether," which is continuous with a bump, termed "tether head," on the *f*α head (Heuser *et al.*, 2012). These tether structures are conserved in *Chlamydomonas* flagella, *Tetrahymena* cilia, sea urchin sperm, and human respiratory cilia (Pigino *et al.*, 2012; Lin *et al.*, 2014).

In this report, we investigated the structure and the function of the IDA *f* using a mutant lacking the tether. Cryoelectron tomography revealed that the IDA *f* undergoes a large conformational change in the absence of the tether. The structural and functional defects in the tether-less mutant suggest that the tether locks the IDA *f* heads in a fixed position and converts the motor power into a modulating force for axonemal bending rather than microtubule-sliding motion.

RESULTS

Characterization of fap44 mutant

The large collection of insertional mutants available from the *Chlamydomonas* Library Project (CLiP) has enabled researchers to easily conduct reverse genetics on the green algae (Li *et al.*, 2016), which is an important model organism for studying cilia and flagella. In combination with the proteomic analysis of *Chlamydomonas* flagellar proteins (Pazour *et al.*, 2005), we searched for conserved axonemal proteins that had not been characterized. Among several candidates, we selected FAP44 (a homologue of mammalian CFAP44/WDR52 [Tang *et al.*, 2017]), because it grouped with known IDA proteins in a cluster analysis of proteins in flagellar fractions (Supplemental Figure S1A) (Pazour *et al.*, 2005). Thus, we obtained a CLiP strain, LMJ.SG0182.019151 (*fap44*), as a possible IDA-defective mutant.

The *fap44* mutant has an insertion of the paromomycin-resistance gene immediately after the start codon (Figure 1A), and the absence of FAP44 protein in the mutant was confirmed by immunoblotting (Figure 1B). The swimming speed is slower than that of wild type (Figure 1C), and the beating motion had a slight reduction in the bend amplitude (Figure 1D). The *fap44* cells showed normal phototactic behavior, while the IDA *f*-missing mutant *ida1* showed no phototaxis (Supplemental Figure S1B). Although the motility defect of *fap44* is mild compared with ODA- or IDA-deficient mutants (e.g., *oda2*, *ida1*, and *ida5*), the immotile phenotype of the *oda2fap44* double mutant indicates a significant defect in the motility-generating machinery of *fap44*. Similarly, sliding disintegration assays showed a significant reduction in the microtubule-sliding activity in the *fap44* axoneme (Figure 1E).

Cryoelectron tomography of the DMT structure of *fap44* showed a large structural defect adjacent to the IDA *f* (Figure 2), while the central pair structure was normal (Supplemental Figure S1C). The missing structures were previously designated as the tether and the tether head (Figure 2, A–C, red) (Heuser *et al.*, 2012). Hereafter, we call the tether and the tether head collectively "tether." Although the IDA *f* and the tether appeared to be associated with each other, the absence of the tether does not affect the assembly of IDA *f* and its IC-LC complex on the DMT. As FAP44 and the tether are present in the IDA *f*-missing mutant (Supplemental Figure S1D) (Heuser *et al.*, 2012; Yamamoto *et al.*, 2017), the axonemal assembly of IDA *f* and the tether are completely independent of each other. Because structural defects in IDA *f* can result in hyperphosphorylation of IC138 (VanderWaal *et al.*, 2011), we examined the phosphorylation state of IC138 in the *fap44* mutant (Supplemental Figure S1E). However, we did not observe a shift in the mobility of the IC138 band in *fap44*. Thus, the motility defect in *fap44* is not associated with IC138 phosphorylation.

Nucleotide-dependent conformational change in IDA *f*

To investigate the reason for the motility defect in the *fap44* mutant, we analyzed the nucleotide-dependent conformational change in IDA *f* (Figure 3 and 4). In ODA and other IDAs, binding of ATP and its hydrolysis cause a release and rebinding of the microtubule-binding domain of the stalk, and a tilt and a shift in the head toward the minus end of the microtubule (Goodenough and Heuser, 1982; Ueno *et al.*, 2008, 2014; Lin *et al.*, 2014). The tilt and the shift in the head collectively cause an 8-nm-sliding per ATP hydrolysis cycle (Movassagh *et al.*, 2010; Lin *et al.*, 2014). In wild-type IDA *f*, the head and the stalk of *f*α showed a tilt, but the *f*β head and stalk did not show evident shift or tilt (Figures 3A and 4A). The direction of the tilt in the *f*α head and stalk is perpendicular to microtubule-sliding direction (Figures 3A and 4A), suggesting that the tilt in the *f*α head and stalk does not contribute to the microtubule sliding along the longitudinal axis (Bui *et al.*, 2008). It is noteworthy that both the *f*α and *f*β stalks point toward the gap between protofilaments B8 and B9 (Figure 4A, green), while other IDA stalks bind to the B-tubule between protofilaments B9 and B10 (Figure 4C) (Bui *et al.*, 2008; Lin *et al.*, 2014).

In the apo structure of the *fap44* axoneme, the orientations of the stalk domains were largely the same as in wild type (Figure 4B), although there is a slight shift toward the ODA in the *f*β head domain (Figure 2B, red broken line). However, the *fap44* mutant showed a large nucleotide-dependent conformational change in IDA *f* (Figures 3B and 4B). As the averaged IDA *f* structure in ATP-plus-vanadate form was unclear due to the great degree of structural heterogeneity, we carried out a principal component analysis to visualize the head and stalk domains (Heumann *et al.*, 2011). There are roughly three structural states in *fap44* IDA *f* with ATP and vanadate; ~45% of the particles belongs to state I, 30% belongs to state II, and the rest of the particles are in state III, which is similar to the apo state. In both states I and II, the *f*β head moves toward the ODA and resides in the position that is occupied by the tether structure in wild-type axoneme (Figures 3B and 4B). The displacement of the *f*β head is larger in state II relative to state I. As the *f*α head lies between *f*β and the B-tubule, it is highly unlikely that the *f*β stalk in states I and II can reach the B-tubule. Therefore, the nucleotide-dependent conformational change in wild-type IDA *f* appears to be mechanically restricted by the tether structure.

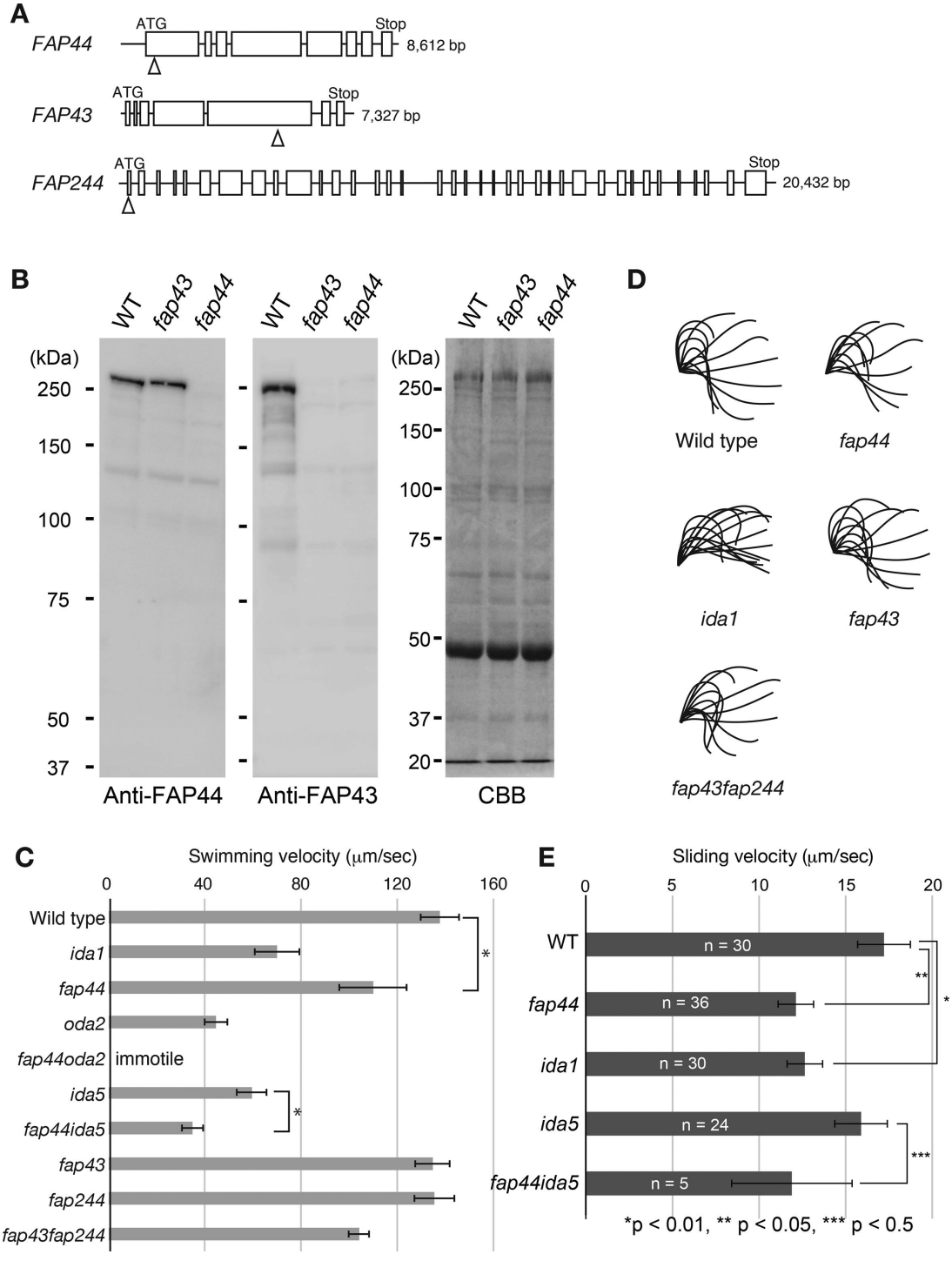

FIGURE 1: Characterization of the *fap44* mutants. (A) Schematic illustrations of the genomic DNA sequences of *FAP44*, *FAP43*, and *FAP244* genes. The boxes and the lines represent the exons and the introns/untranslated regions, respectively. The arrowheads indicate the position of the paromomycin-resistance gene cassettes inserted for the mutagenesis. (B) Immunoblots showing the absence of FAP44 protein in the *fap44* axoneme. The *fap43* mutant retained the FAP44 protein. (C) Swimming velocities of the wild-type and the mutant strains. The *fap44* cells showed reduced motility. Asterisks indicate statistically significant differences ($p < 0.01$, Student's *t* test). No swimming cells were observed in the *fap44oda2* double mutant. Means ± SD for the swimming velocities were calculated from 20 cells. (D) Waveforms of the wild-type and the mutant strains. The *fap44* flagella showed a slight reduction in the bend amplitude. (E) Sliding disintegration assay of the axoneme. Microtubule sliding velocities were measured by observing the sliding of protease-treated and ATP-activated axonemes. Means ± SEM for the sliding velocities were calculated from indicated number of sliding events. The *fap44* axoneme showed reduced microtubule sliding activity. Asterisks indicate the corresponding probability values calculated by Student's *t* test. Although there is no statistically significant difference between the sliding velocities of *ida5* and *fap44ida5* axonemes, few sliding events were observed in *fap44ida5* (thus, *n* is only 5), suggesting a motility defect in the double mutant.

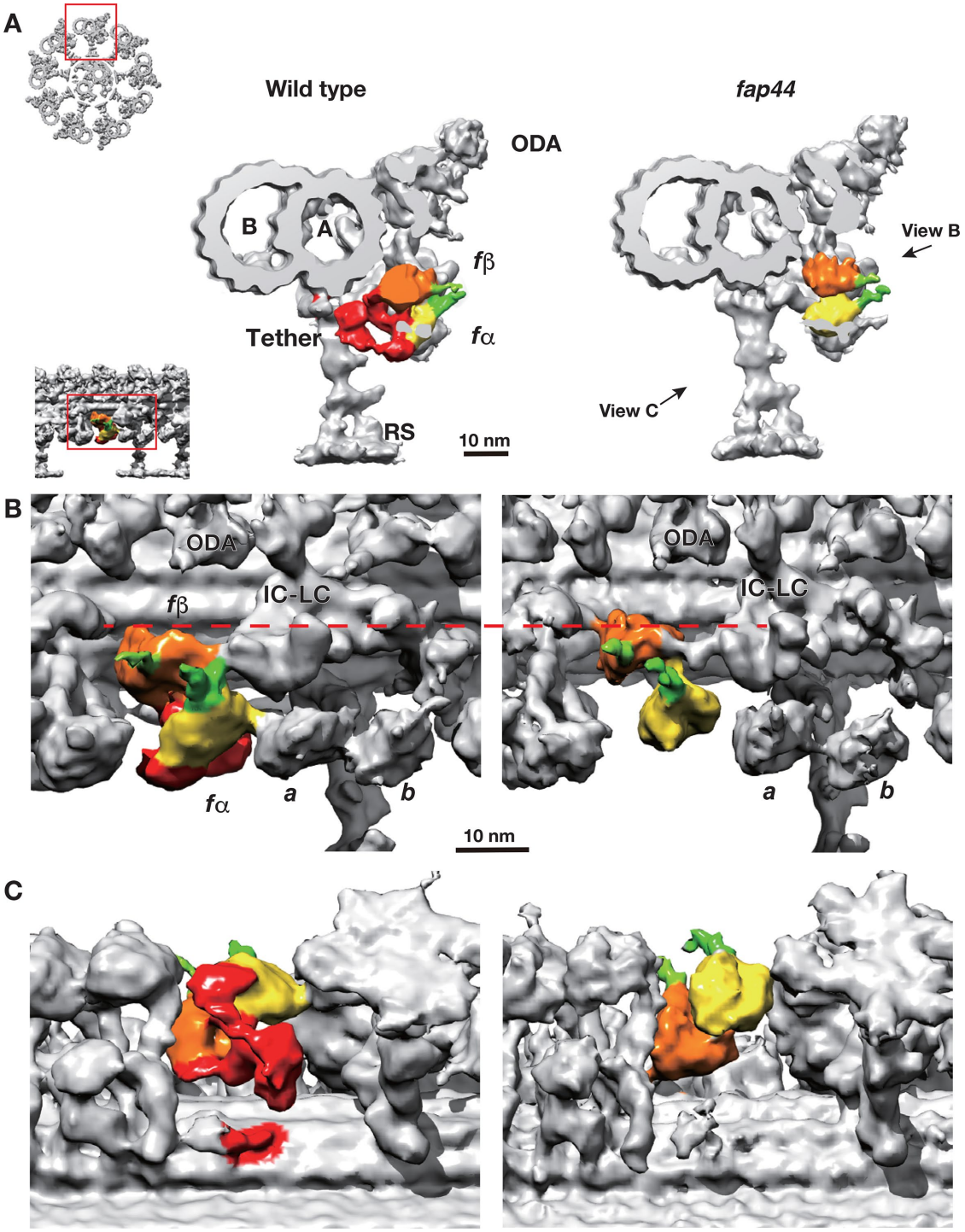

FIGURE 2: *fap44* axoneme lacks the tether. (A) Cross-sectional views of the three-dimensional structure of the axoneme. The upper left inset is the base-to-tip view of the 9+2 structure. The red box indicates the position of the enlarged DMTs on the right. Red: tether; yellow: *f*α head; orange: *f*β head; green: stalks. The directions of the views in B and C are indicated. RS: radial spoke; A and B: A-tubule and B-tubule, respectively. (B, C) Longitudinal views of the IDA *f*. The tether in red is missing in the *fap44* axoneme. Red broken line indicates the shift in the *f*β head toward the ODA. IC-LC: the IC-LC complex of the IDA *f*; *a* and *b*: the IDA subspecies *a* and *b*, respectively. The DMT structures are oriented with the distal ends on the right.

FAP43 and FAP244 are components of the tether

The large volume of the missing density in the *fap44* structure suggested that the tether contains proteins in addition to FAP44. Thus, we conducted quantitative mass spectrometry analyses to compare the protein compositions of wild-type and *fap44* axonemes (Table 1). In addition to FAP44, we found that several other proteins, including FAP43, FAP102, FAP244, Cre10.g452250, and a smaller protein, MOT7, are missing or greatly reduced in the *fap44*

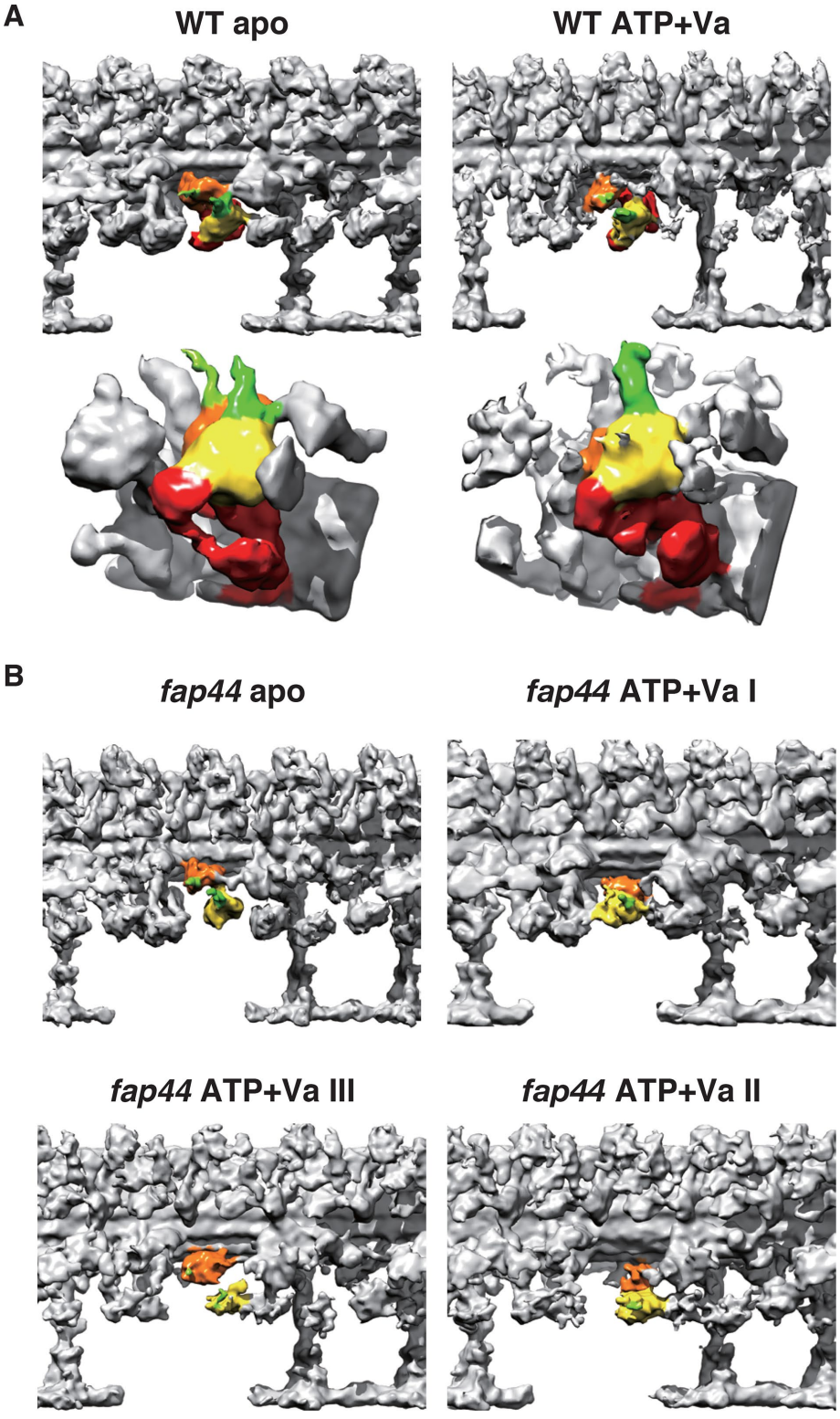

FIGURE 3: Nucleotide-dependent conformational change of IDA *f* in three dimensions. The IDA *f* structures in the apo and the ATP plus vanadate (ATP+Va) states. (A) Wild type and (B) *fap44* mutant. Red: tether; yellow: *f*α head; orange: *f*β head; green: stalks. (A) The head and the stalk of the *f*β show a tilt vertical to the long axis. (B) There are three states (I, II, and III) in the conformation of the IDA *f* in the presence of ATP+Va. Both *f*α and *f*β heads show a large displacement away from the ODA.

axonemes. MOT7, FAP102, and Cre10.g452250 will not be discussed further here. Interestingly, FAP43, FAP44, and FAP244 are predicted to share the same domain organization: two tryptophan-aspartic acid (WD)-repeat domains in the amino-terminal half and several coiled-coil domains in the carboxy-terminal half (Figure 5A). Therefore, we obtained two more CLiP strains LMJ.SG0182.005221 (*fap43*) and LMJ.RY0402.124246 (*fap244*), which have disruptions in the *FAP43* and *FAP244* genes, respectively (Figure 1A).

To our surprise, the DMT structures of both *fap43* and *fap244* axonemes appeared the same as the wild type with normal tether structures (Figure 5B). We examined the interspecies conservation of the two proteins and found that the *FAP43* gene is conserved across species including mammals (*CFAP43*/*WDR96*), while the *FAP244* gene is conserved only among Chlorophyceae. The weak sequence similarity between FAP43 and FAP244 proteins suggested that FAP43 and FAP244 are functionally redundant. To test this hypothesis, we made a double mutant *fap43fap244* and found that it is an exact phenocopy of *fap44*; it lacks the tether structures and FAP44 protein (Figure 5, B and C). We expressed the FAP43 protein tagged with a biotin carboxyl carrier protein (BCCP) at the carboxy-terminus in the *fap43fap244* mutant and confirmed the recovery of FAP44 protein (Supplemental Figure S2A, *FAP43C*) and the tether structure (Figure5B,*fap43fap244:fap43fap244:FAP43-C-BCCP*). These results indicate that the tether structure contains FAP44 and FAP43/FAP244 proteins and that FAP43 and FAP244 can compensate for each other.

Interestingly, the immunostaining with an anti-FAP43 antibody revealed that FAP43 is missing in the proximal one-fifth of the wild-type axoneme (Figure 6, right, red arrowheads). In contrast, FAP43 localizes along the whole length of the *fap244* axoneme. These results suggest a functional differentiation between the two proteins: FAP43 and FAP244 localize to distal and proximal parts of the axoneme, respectively, but in the absence of FAP244, FAP43 replaces it in the proximal part. Moreover, labeling by the anti-FAP44 antibody staining was diminished at the distal tip of the *fap43* flagella (Figure 6, left, white arrowheads). This result suggests that FAP244 may not be able to substitute for FAP43 at the distal tip of the *fap43* axoneme and thus fails to recruit FAP44 in this region.

Structural configuration and composition of the tether

To investigate the molecular configuration of the tether structure, we rescued the *fap44* and *fap43fap244* mutants with constructs designed to express FAP44 and FAP43 fused to the BCCP tag (Oda and Kikkawa, 2013). To avoid disruption of functional domains such as WD domains and

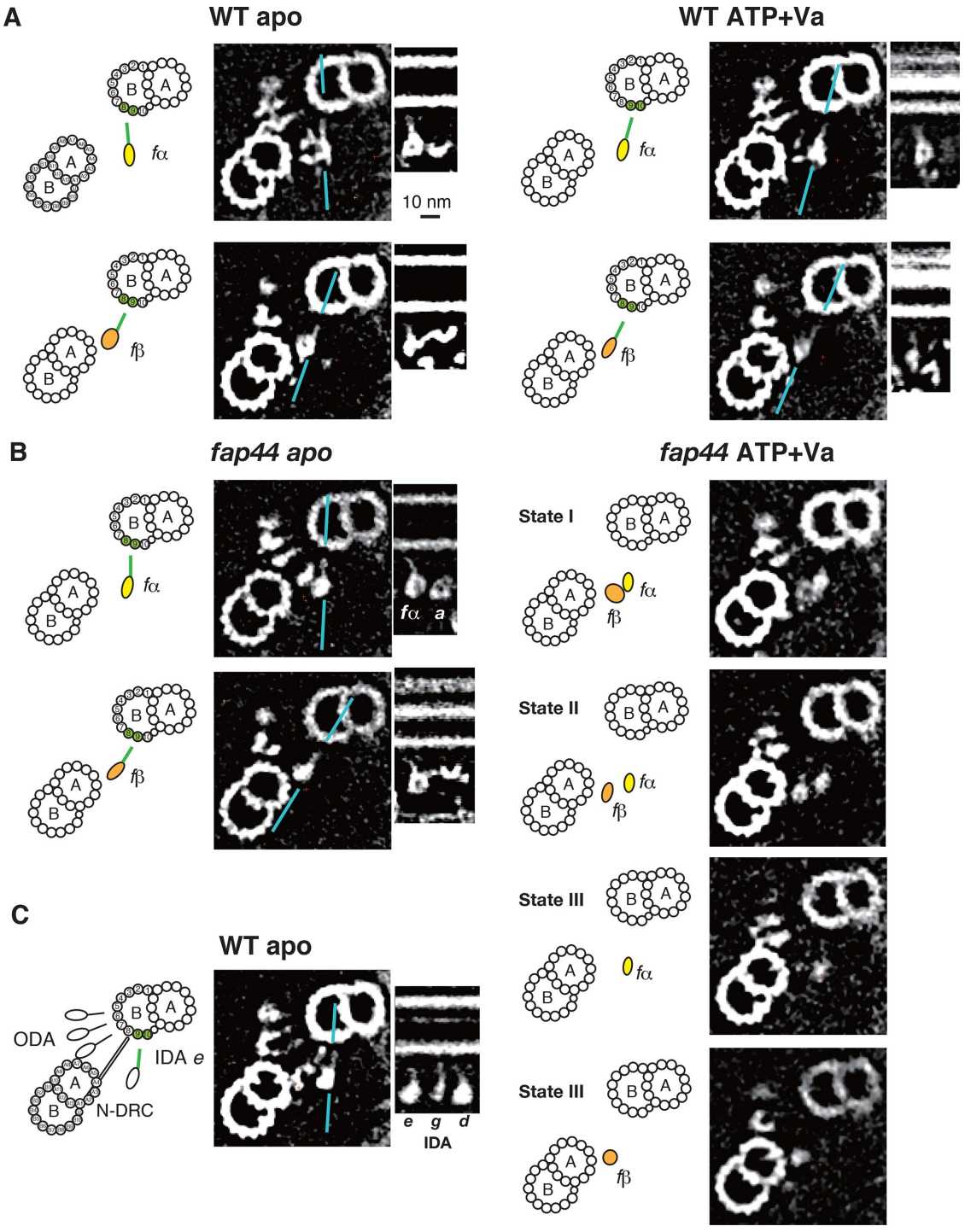

FIGURE 4: Two-dimensional slice representations of the nucleotide-dependent conformational change in IDA *f*. (A) Wild type and (B) *fap44* mutant. Cross-sections are in base-to-tip views. Schematics showing the DMT, heads, and stalks are displayed on the left of the corresponding cross-sections. Yellow: *f*α head; orange: *f*β head; green: stalk. Longitudinal sections, with the distal ends on the right, are placed next to the cross-sections. The orientations of the longitudinal sections are indicated with blue lines. Protofilaments in green indicate the expected position of the microtubule binding domain of the stalk. (C) Head and stalk orientations of the ODA and IDA *e* are shown in cross- and longitudinal sections.

coiled-coils (Figure 5A), we inserted the BCCP-tag immediately after Ser43 (*FAP44N*) or Thr2089 (*FAP44C*) of FAP44 and at the carboxy-terminus of FAP43 (*FAP43C*). Ser43 of FAP44 is located within the predicted Duffy antigen-binding domain, but this domain is predicted to be largely disordered (Jones and Cozzetto, 2015). We then isolated the axonemes and labeled them with streptavidin and biotinylated cytochrome *c* (Oda *et al.*, 2014; Oda, 2017).

Cryoelectron tomography of the labeled axonemes revealed that FAP44 has an elongated conformation spanning from the *f*β head to the RS3 stump (Figure 7, left). The carboxy-terminus of

	Predicted mass (kDa)	Fold change	Top 3 Precursor Intensity in *fap44*	Top 3 Precursor Intensity in WT
FAP44	222	0	0	1.79E+09
MOT7	26	0	0	7.81E+08
FAP244	267	0	0	5.53E+08
FAP43	199	0.02	2.11E+07	1.27E+09
Cre10.g452250	68	0.03	2.36E+07	8.87E+08
FAP102	156	0.08	4.05E+07	4.99E+08

"Top 3 Precursor Intensity" is a measure of protein abundance and is a unit-less number (Silva *et al.*, 2006). Cre10.g452250 is a Phytozome ID in the *Chlamydomonas reinhardtii* Joint Genome Institute v5.5 genome assembly (Goodstein *et al.*, 2012); the NCBI accession number for this protein is XP_001698522. No significant mammalian homologues were found for Cre10.g452250 and FAP102.

TABLE 1: Known or predicted flagellar proteins missing or greatly reduced in the *fap44* axoneme.

FAP43 also is located near the RS3 stump (Figure 7, right). These results suggest that the amino-terminal domain of FAP44, and probably the amino-terminal domain of FAP43, comprises a large part of the tether structure, while the carboxy-terminal coiled-coils of FAP44 and FAP43 form an anchor to the microtubule. The positions of the carboxy-termini of both FAP44 and FAP43 coincide with the interprotofilament gap, along which the 96-nm ruler complex runs (Oda *et al.*, 2014). It is possible that the position of the tether complex in the 96-nm repeat is determined by the interaction between the ruler complex and the carboxy-terminal coiled-coils of FAP44 and FAP43.

IDA f, FAP44, and FAP43 form a complex

To confirm the interaction between IDA *f* and the tether complex, we purified IDA *f*, FAP44, and FAP43 using ion exchange chromatography and performed an immunoprecipitation assay. All three

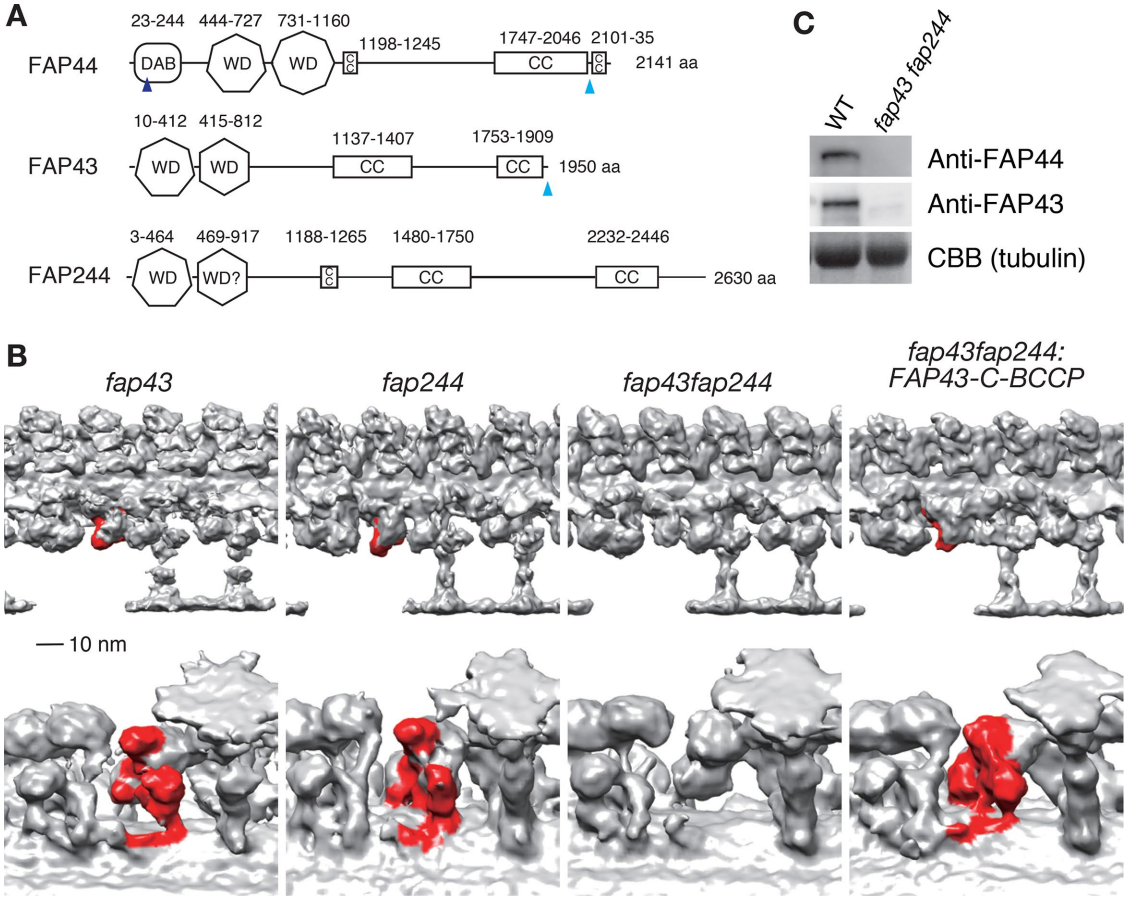

FIGURE 5: Functional redundancy between FAP43 and FAP244. (A) Schematic illustrations showing the domain organizations of FAP44, FAP43, and FAP244. DAB: Duffy antigen-binding domain; WD: WD domain (polygons represent the number of WD repeats); CC: coiled-coil domain. "WD?" in FAP244 indicates low confidence in the assignment of the WD domain due to the degeneration of the motif sequences. Blue arrowheads indicate the positions of the BCCP tags. (B) Three-dimensional structure of the DMT. *fap43* and *fap244* retain the tether structure (red), while *fap43fap244* mutant lacks the tether. Expression of BCCP-tagged FAP43 restored the tether in *fap43fap244*. (C) Immunoblots showing that the *fap43fap244* double mutant lacks *fap44*.

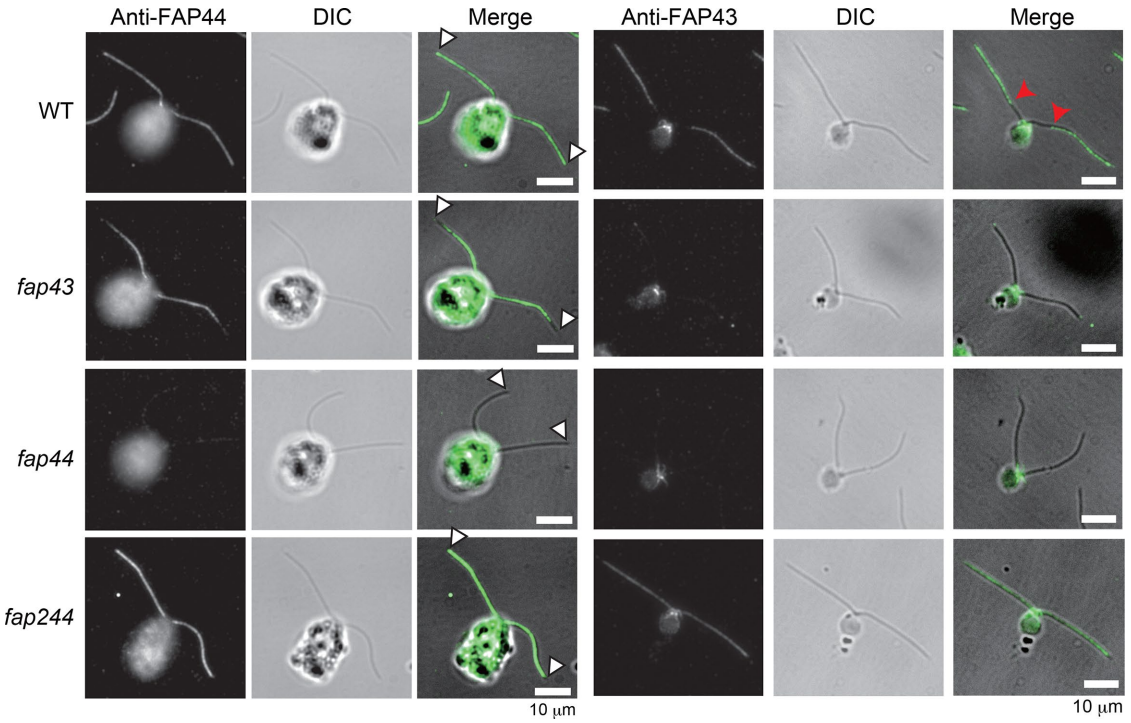

FIGURE 6: Immunolocalization of FAP44 and FAP43 within the axoneme. The nucleoflagellar apparatus were stained with anti-FAP44 or anti-FAP43 antibody. White arrowheads indicate the distal ends of the flagella. FAP44 staining in the *fap43* flagella is diminished near the distal ends. Red arrowheads indicate the proximal regions of the wild-type flagella lack FAP43 staining. In contrast, the whole lengths of the *fap244* flagella were stained with anti-FAP43 antibody.

components comigrate on the anion exchange column (Figure 8A), and IDA *f* and FAP43 were coimmunoprecipitated with BCCP-tagged FAP44 (Figure 8B). These results indicate that FAP44 forms a complex with IDA *f* and FAP43.

To characterize the association of FAP44 and FAP43 with the axoneme, we performed fractionations of axonemal proteins using various concentrations of sarkosyl (Figure 8C) (Witman *et al.*, 1972). We found that some of FAP44 and FAP43 dissociated from the wild-type axoneme even without the detergent treatment, although the majority of the proteins required 0.2% sarkosyl for extraction. Even more of the proteins were extracted without sarkosyl in *fap43* and *fap244* axonemes, and the majority of the proteins were extracted with 0.1% sarkosyl in these mutants. These results suggest that the tether structures are relatively unstable or susceptible to spontaneous degradation and that the absence of FAP43 or FAP244 further destabilizes the complex even though FAP43 and FAP244 are thought to compensate each other.

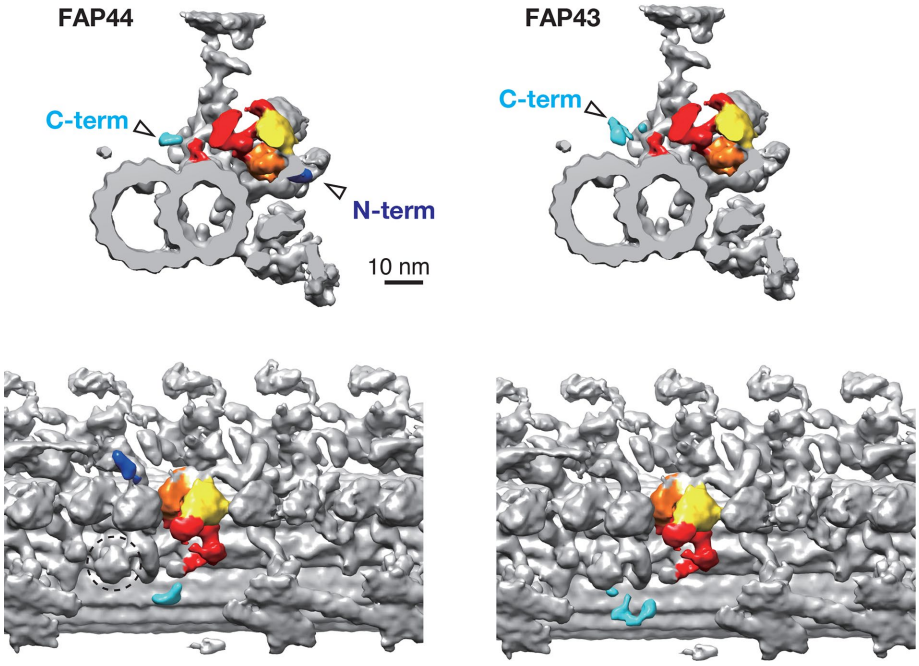

FIGURE 7: Three-dimensional localizations of the termini of FAP44 and FAP43. Top, Tip-to-base view; bottom, distal end on the right. Tag densities were visualized by comparing the wild-type and labeled DMT structures. The broken circle indicates the RS stump (Pigino *et al.*, 2011). Colored densities correspond to positions of the labels indicated by arrowheads of the same color in Figure 5A.

DISCUSSION

The IDA *f* is a mysterious dynein; its in vitro microtubule gliding activity is quite low, and it appears to impede the microtubule sliding of other IDAs, whereas the IDA *f*-missing mutant exhibits a slow-swimming phenotype and IDA *f*-missing axonemes show reduced microtubule sliding (Figure 1, D and E) (Smith and Sale, 1991; Kagami and Kamiya, 1992; Kotani *et al.*, 2007; Toba *et al.*, 2011). One possible explanation for this discrepancy is that the IDA *f* acts as a "brake" on microtubule sliding and modulates the

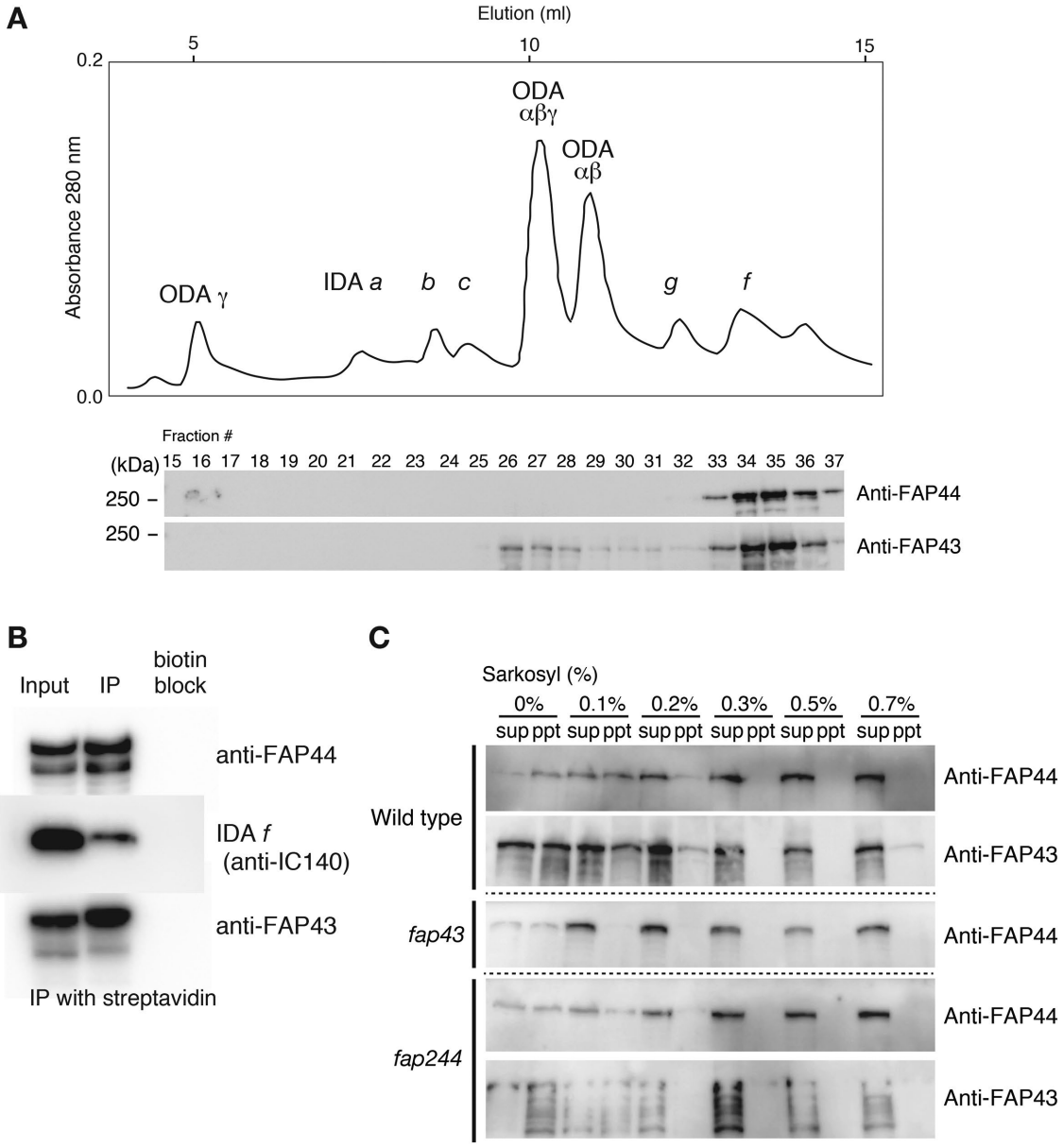

FIGURE 8: Biochemical characterization of the tether complex. (A) Chromatographic separation of the axonemal salt extracts from *FAP44C* strain using an UnoQ anion-exchange column. The dynein species of each peak was identified according to the previous study (Furuta *et al.*, 2009). FAP44 and FAP43 were detected using immunoblotting. Comigration of IDA *f* with FAP44 and FAP43 was clearly observed. (B) Immunoprecipitation of the FAP44 protein. Fractions containing purified IDA *f*, FAP44, and FAP43 were collected and BCCP-tagged FAP44 proteins were immunoprecipitated (IP) using streptavidin-agarose. As a negative control (biotin block), the streptavidin-agarose was blocked with 1 mM biocytin (biotin-lysine). IDA *f* was detected using the IC140 antibody. IDA *f* and FAP43 were co-immunoprecipitated with FAP44. (C) Sarkosyl fractionation of axonemal proteins. Axonemal proteins were extracted with various concentration of sarkosyl. Supernatant (sup) and precipitate (ppt) after centrifugation were analyzed by immunoblotting. Although the phenotypes of *fap43* and *fap244* are virtually wild type, extraction patterns showed destabilization of the tether complex.

bending waves. Another possibility is that the manifestation of the full motor activity of IDA *f* requires the whole complex, including the tether and the IC-LC complex, to be aligned in the right position and configuration, which is unlikely to happen in the in vitro assay. Our structural results partially support the first hypothesis: in the presence of ATP and vanadate, the *f*α and *f*β heads did not show a significant shift but the *f*α stalk changed its microtubule-binding site from the B8-B9 to the B9-B10 protofilaments (Figures 4A and 9). This nucleotide-dependent conformational change in IDA *f* does not seem to contribute to the microtubule sliding in the longitudinal direction, but it is possible that the circumferential tilt of the *f*α head and stalk modulates the direction of the forces that other dyneins generate. What is the function of the *f*β, then? The in situ microtubule sliding activity measured by the axonemal disintegration assay (Toba *et al.*, 2011) suggests that the *f*β mostly accounts for the motor activity of the IDA *f*. In our structural data, the *f*β showed a large conformational change in the absence of the tether structures. This result suggests a "jostling" model that, in the wild-type axoneme,

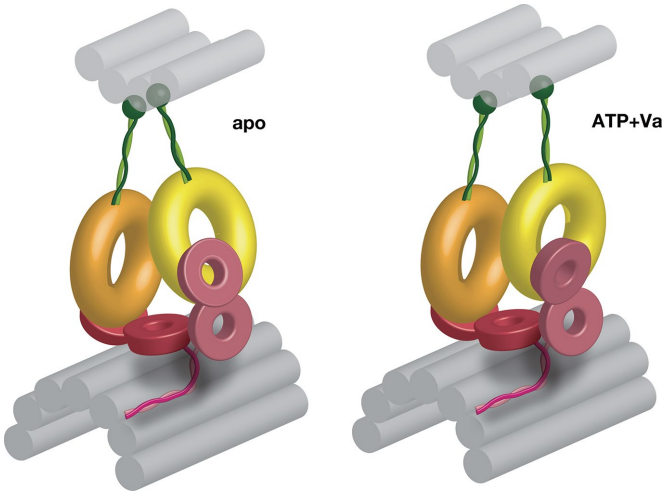

FIGURE 9: Schematic models of the IDA *f*-tether complex. Yellow ring: *f*α head; orange ring: *f*β head; green strings: stalks; green sphere: stalk heads (microtubule binding domains of IDA *f*); red rings: WD domains of FAP44 and FAP43; red strings: coiled-coil domains of FAP44 and FAP43; gray tubes: protofilamens of the axonemal microtubules. The tether complex is thought to be a heterodimer of FAP44 and FAP43 bundled via their carboxy-terminal coiled-coil domains, which are anchored to the A-tubule or to the 96-nm ruler complex. The tether complex holds both *f*α and *f*β heads, and the nucleotide-dependent movement of the IDA *f* is restricted to a tilt in the *f*α head and stalk, which brings the microtubule binding domain to the adjacent protofilament.

the *f*β attempts to exert a power stroke, but the tether structures constrain the *f*β to be stationary. The stationary *f*β does not necessarily mean that the motor is wasting energy, but it can be involved in other activities, such as applying tension to the IC-LC complex or the MIA structure or direct collision with the adjacent IDA. Similarly, the *f*α head may be involved in the collision-based motility regulation because the apparent connection between the *f*α and IDA *a* was missing in *fap44* mutant structure (Figure 2B). This result suggests that the tether mediates a functional interaction between the *f*α and IDA *a*. Further structural and biochemical studies are necessary to identify the precise function of the IDA *f*.

Recently, Tang *et al.* (2017) reported that biallelic mutations in the mammalian homologue of FAP44 and FAP43 (CFAP44 and CFAP43, respectively) cause morphological abnormality in human sperm flagella, resulting in male infertility. In *Chlamydomonas fap44* flagella, we did not observe flagellar length defect or axonemal disorganization. The severe phenotype in human sperm flagella can be attributed to the function of a CFAP44 splice variant, which is reportedly involved in the regulation of cytoplasmic microtubule dynamics (Tanaka and Tanaka, 2017). The immotile phenotype of *fap44oda2* mutant (Figure 1C) may be related to the severe structural defect in mammalian sperms lacking FAP44. It is known that simultaneous loss of multiple axonemal structures, such as ODA, IDA, and radial spokes, causes short and immotile flagella (Piperno *et al.*, 1990; Kubo *et al.*, 2015; Lin *et al.*, 2015). It is possible that the simultaneous loss of the tether and the ODA in *fap44oda2* mutant destabilizes the axonemal microtubules. We also found that *fap44ida7* (Table 1; *ida7* lacks the whole IDA *f* complex) showed immotile phenotype. These results suggest that the tether structure is important for the stabilization of the axonemal microtubules, especially in mammalian sperm.

The characteristic domain organization of FAP44 and FAP43, the WD domains and the coilded-coils, is similar to the structure of another dynein regulator, Lis1 (McKenney *et al.*, 2010; Huang *et al.*, 2012; Rompolas *et al.*, 2012). Lis1 has a seven-propeller WD domain at its carboxy-terminus and forms a homodimer through the amino-terminal coiled-coil. Lis1 binds to the AAA5 domain of the cytoplasmic dynein head via the WD domain (Toropova *et al.*, 2014). Binding of Lis1 to the dynein head inhibits the power stroke by mechanically blocks the swing in the linker region of the tail domain. In contrast to Lis1, which binds to the dynein near the root of the stalk, the tether appears to bind to the *f*α head at the opposite side to the stalk (Figures 2 and 3). This position corresponds to the AAA1 domain, which is the major catalytic domain of the ATP hydrolysis (Gibbons and Gibbons, 1987; Kon *et al.*, 2004). It is an interesting question whether the tether regulates the motor activity of IDA *f* by modulating the motion of the tail like Lis1 or altering the ATP hydrolysis in the AAA1. To investigate the molecular mechanism of the tether-mediated regulation, it is necessary to further improve the resolution of the three-dimensional structure of the IDA *f*-tether complex.

MATERIALS AND METHODS

Strains and reagents

Chlamydomonas reinhardtii cells were grown in Tris-acetate-phosphate (TAP) medium. To screen transformants, cells were grown on TAP agar supplemented with hygromycin B (20 μg/ml; Nacalai Tesque, Kyoto, Japan). The *fap44* (LMJ.SG0182.019151), *fap43* (LMJ.SG0182.005221), and *fap244* (LMJ.RY0402.124246) mutant strains were obtained from the CLiP Library (Li *et al.*, 2016). The CliP strains were back-crossed with the wild-type strain at least five times before the experiments. *Chlamydomonas reinhardtii* strains used in this study are listed in Table 2. For generation of anti-FAP44 and FAP43 antibodies, cDNA sequence encoding the amino acids 1-271 of FAP44 and 689-1312 of FAP43 were each inserted into the pGEX-6p-2 plasmid and polypeptides were expressed in *Escherichia coli* cells. Anti-FAP44 and FAP43 rabbit polyclonal antibodies were then raised against the purified proteins. Anti-DRC3 and anti-IC140 antibodies were generated in the previous studies (Oda *et al.*, 2014, 2015). Anti–human influenza hemagglutinin (HA) antibody 4B2 was purchased from Wako Pure Chemical Industries (Tokyo, Japan). Anti-IC138 antisera was a kind gift from W. S. Sale (Emory University, Atlanta, GA).

Preparation of axonemes

Chlamydomonas cells were deflagellated with dibucaine-HCl (Nacalai Tesque), and axonemes were collected by centrifugation (Piperno *et al.*, 1977). Flagella were demembranated with 1% Nonidet P-40 (NP-40) in HMDENa buffer or HMDEK buffer composed of 30 mM HEPES-NaOH, pH 7.2, 5 mM $MgCl_2$, 1 mM dithiothreitol (DTT), 1 mM ethylene glycol tetraacetic acid, 50 mM NaCl (HMDENa), or 50 mM CH_3COOK (HMDEK), and 1× Protease inhibitor cocktail (Nacalai Tesque). To observe the phosphorylation state of IC138, cells were deflagellated with acetic acid, and trichloroacetic acid (final 5% vol/vol) was immediately added to fix the phosphorylation state of the axonemal proteins (Wakabayashi and King, 2006). Cells bodies were removed by differential centrifugation, and flagella were pelleted and washed three times with acetone. Dried flagella were resuspended in urea–SDS sample buffer (50 mM Tris-HCl, pH 6.8, 2% SDS, 8 M urea, and 2% 2-mercaptoethanol) and boiled for 10 min. Axonemal proteins were resolved by SDS–PAGE on 5–15% polyacrylamide gradient gels (Nacalai Tesque) and then blotted onto polyvinylidene difluoride membranes. Blots were probed with the indicated primary antibodies.

Strains	Abbreviations	Mutated genes	Missing structures	References
Wild-type CC-125				
oda1		*DC2*	ODA, ODA-DC	Kamiya, 1988
oda2		*ODA γ*	ODA	Kamiya, 1988; Koutoulis *et al.*, 1997
ida1		*DHC1*	IDA *f*	Kamiya *et al.*, 1991
ida4		*p28*	IDA *a*, *c*, *d*	Kagami and Kamiya, 1992; LeDizet and Piperno, 1995
ida5		*actin*	IDA *a*, *c*, *d*, *e*	Kato *et al.*, 1993
ida7		*IC140*	IDA *f*	Perrone *et al.*, 1998
pf18			Central pair	Adams *et al.*, 1981
LMJ.SG0182.019151	*fap44*	*FAP44*	Tether	CLiP
fap44oda2				This study
fap44ida5				This study
fap44ida7				This study
fap44:FAP44-N-BCCP	*FAP44N*			This study
fap44:FAP44-C-BCCP	*FAP44C*			This study
LMJ.SG0182.005221	*fap43*	*FAP43*		CLiP
LMJ.RY0402.124246	*fap244*	*FAP244*		CLiP
fap43fap44			Tether	This study
fap43fap244:FAP43-C-BCCP	*FAP43C*			This study

TABLE 2: Strains used in this study.

Construction of the expression vectors

Fragments spanning from the start codon to immediately before the stop codon for genes encoding FAP44 and FAP43 were amplified with genomic PCR using genomic DNA from the wild-type strain CC-125 and were then inserted into pIC2 plasmids (Oda *et al.*, 2015). We inserted the tag sequence corresponding to amino acids 141–228 of *Chlamydomonas* BCCP in the middle of the sequences of FAP44 between Asp42 and Ser43 (FAP44-N-BCCP) or between Ala2099 and Thr2089 (FAP44-C-BCCP) or after the last residue of FAP43, Thr1950 (FAP43-C-BCCP). Expression of the tagged proteins were confirmed by immunoblotting (Supplemental Figure S2A) and immunocytochemistry (Supplemental Figure S2B).

Fluorescence microscopy detection of axonemes

For fluorescence staining using streptavidin, demembranated axonemes were attached to glass slides and blocked with 1 mg/ml bovine serum albumin (BSA) in HMDEK buffer. Axonemes were incubated with 1 μg/ml Alexa Fluor 546-conjugated streptavidin (Invitrogen, Carlsbad, CA) for 1 min. Labeled axonemes were washed three times with HMDEK buffer before observation. For immunostaining using antibodies, nucleoflagellar apparatuses prepared by the previously described method (Taillon and Jarvik, 1995) were fixed with 2% formaldehyde for 10 min at room temperature, followed by treatment with cold acetone and methanol (–20°C). Fixed samples were immunostained by the previously described method (Sanders and Salisbury, 1995). Stained axonemes were observed using a fluorescence microscope (BX53; Olympus, Tokyo, Japan). Images were recorded using a charge-coupled device (CCD) camera (ORCA-Flash4.0; Hamamatsu PhotonICs, Hamamatsu, Japan).

Measurement of swimming velocity

The swimming velocity of *Chlamydomonas* cells was recorded using a BX53 microscope (Olympus) at a total magnification of ×100. A red filter with a cutoff wavelength of 630 nm was inserted before the condenser lens to suppress the cellular response to light.

Waveform analysis

Chlamydomonas cells were observed using a dark-field microscope (BX53, Olympus), and images were captured using a high-speed digital camera (EXILIM EX-F1; Casio, Tokyo, Japan) at 600 frames/s. Cells whose flagella were well in focus were selected, and the shapes of flagella were manually traced using Adobe Illustrator.

Sliding disintegration of the axoneme

To measure the sliding velocity, suspension of flagella was sonicated using a Q125 sonicator (Qsonica LLC, Newtown, CT). Sonication was repeated until the flagella were sheared in half lengthwise on average. The flagella were then demembranated with 1% NP-40 in HMDEK buffer and centrifuged. Axonemes were resuspended in HMDEKP (HMDE with 25 mM potassium acetate and 1% polyethylene glycol [20,000 MW]) buffer and absorbed onto a glass slide. The solution was covered with a coverslip with its two sides sealed with strips of double-stick tape. Axonemes were activated with HMDEKP with 1 mM ATP. Sliding disintegration was initiated by washing the flow chamber with HMDEKP with 1 mM ATP and 2 μg/ml nagarase (Sigma-Aldrich). Sliding of DMTs was observed using a dark-field microscope (BX53, Olympus) equipped with a ×50 oil-immersion objective lens and a 100-W mercury lamp. The image sequences were recorded using a CCD camera (M-3204C, Olympus).

Sample preparation for cryoelectron tomography

Streptavidin-cytochrome *c* labeling of BCCP-tagged axonemes was carried out as described previously (Oda *et al.*, 2014) with minor modifications. Demembranated axonemes were incubated with 0.05 mg/ml streptavidin for 15 min at 4°C in HMDENa buffer in the presence of 1 mg/ml BSA. Next, axonemes were washed

and incubated with 0.05 mg/ml biotinylated cytochrome *c*. This sequence was repeated, so that the biotinylated Fab fragments were labeled with three rounds of streptavidin and two rounds of cytochrome *c*. Labeled or unlabeled axonemes were resuspended in HMDENa buffer at a concentration of 0.02 mg/ml and mixed with cationic 15-nm colloidal gold (BBI Solutions, Cardiff, UK). Both side of homemade holey carbon grids were glow-discharged for 20 s. Suspended axonemes plus colloidal gold (5 µl) was loaded onto the grids and plunge-frozen in liquid ethane at –180°C with a Vitrobot Mark IV automated plunge-freezing device (FEI, Hillsboro, OR).

Image acquisition

Grids were transferred to a JEM-3100FEF or JEM-2100F transmission electron microscope (JEOL, Tokyo, Japan) with a Gatan 914 (3100FEF) or 626 (2100F) high-tilt liquid nitrogen cryotransfer holder (Gatan, Pleasanton, CA). Tilt series images were recorded at –180°C using Gatan K2 summit direct detector (3100FEF) or a TemCam-F216 CMOS camera (2100F; TVIPS, Gauting, Germany) and automated acquisition was performed using SerialEM software (3100FEF) (Mastronarde, 2005) or EM-TOOLs program (2100F; TVIPS). The angular range of the tilt series was from –60° to 60° (3100FEF) or –45° to 45° (2100F) with 2.0° increments. The total electron dose was limited to ~100 $e^-/Å^2$. Images were recorded at 300 keV, with 6–9 µm defocus (3100FEF) or 200 keV with 3- to 5-µm defocus (2100F), at a magnification of ×7100 and a pixel size of 7 Å (3100FEF) or ×19,500 and a pixel size of 8 Å (2100F). With JEM-3100FEF, an in-column omega energy filter was used to enhance image contrast in the zero-loss mode with a slit width of 40 eV.

Image processing

Image processing for subtomogram averaging of DMT structures was carried out as described previously (Oda and Kikkawa, 2013; Oda *et al.*, 2014). Tilt series images were aligned and back-projected to reconstruct three-dimensional tomograms using the IMOD software package (Kremer *et al.*, 1996). Tomograms of intact axonemes with a high signal-to-noise ratio were selected and used for subtomogram averaging of the 96-nm repeats of DMTs. Alignment and averaging of subtomograms were conducted using custom Ruby-Helix scripts (Metlagel *et al.*, 2007) and the PEET software suite (Nicastro *et al.*, 2006). The numbers of DMT subtomograms averaged are summarized in Table 3. The effective resolutions determined by Fourier shell correlation with a cutoff value of 0.5 were ~4 nm (3100FEF) and ~6 nm (2100F) (Supplemental Figure S2C). For principal component analysis, a mask volume enclosing two heads of the IDA f was imposed and top three features were selected for clustering into four classes.

Surface renderings were generated using UCSF Chimera (Pettersen *et al.*, 2004). The EM maps of averaged DMT are available at the EM Data Bank (www.emdatabank.org) under the accession numbers EMD-6866-6874.

Statistical analysis

To identify statistically significant differences, we applied Student's *t* test to compare wild-type and streptavidin-labeled axonemes as described previously (Oda and Kikkawa, 2013; Oda *et al.*, 2014). First, wild-type and streptavidin-labeled subtomograms were randomly divided into three data sets. Subtomograms for each data set were aligned and averaged, and a total of six averaged subtomograms were created. We calculated the *t* value for each voxel and presented it as a single *t*-value map. The isosurface threshold values were $t > 7.17$, with a one-tailed probability of <0.1%.

Label-free quantitation by mass spectrometry

Sample preparation. The proteins in 20 µg of axonemes from wild-type and *fap44* cells were separated on 4–15% SDS–polyacrylamide gels. Each lane was cut into five fractions, and each fraction was processed separately as described. Gel fractions were cut into 1 × 1-mm pieces and placed in 1.5-ml Eppendorf tubes with 1 ml of water for 30 min. The water was removed and 200 µl of 250 mM ammonium bicarbonate was added. For reduction 20 µl of a 45 mM solution of DTT was added and the samples were incubated at 50°C for 30 min. The samples were cooled to room temperature and then for alkylation 20 µl of a

	# of tomograms	# of particles	Microscope+camera
Wild-type apo	10	1460	3100FEF+K2
Wild-type ATP+Va	9	1503	3100FEF+K2
fap44 apo	17	2457	3100FEF+K2
fap44 ATP+Va	12	2250 State I: 765 State II: 499 State III: 436	3100FEF+K2
fap43	8	1216	2100F+F216
fap244	10	1224	2100F+F216
fap43fap244	13	1449	2100F+F216
FAP44N	13	2277	3100FEF+K2
FAP44C	9	1197	2100F+F216
FAP43C	17	2070	2100F+F216
Wild-type central pair	10	688	3100FEF+K2
fap44 central pair	17	966	3100FEF+K2

TABLE 3: Summary of averaged subtomograms.

100 mM iodoacetamide solution was added and allowed to react for 30 min. The gel slices were washed 2× with 1-ml water aliquots. The water was removed, 1 ml of 50:50 (50 mM ammonium bicarbonate: acetonitrile) was placed in each tube, and samples were incubated at room temperature for 1 h. The solution was then removed and 200 µl of acetonitrile was added to each tube, at which point the gels slices turned opaque white. The acetonitrile was removed, and gel slices were further dried in a Speed Vac (Savant Instruments). Gel slices were rehydrated in 100 µl of 4 ng/µl of sequencing grade trypsin (Sigma) in 0.01% ProteaseMAX Surfactant (Promega): 50 mM ammonium bicarbonate. Additional bicarbonate buffer was added to ensure complete submersion of the gel slices. Samples were incubated at 37°C for 18 h. The supernatant of each sample was then removed and placed in a separate 1.5-ml Eppendorf tube. Gel slices were further extracted with 200 µl of 80:20 (acetonitrile: 1% formic acid). The extracts were combined with the supernatants of each sample. The samples were then completely dried down in a Speed Vac.

LC/MS/MS analysis. Tryptic peptide digests were reconstituted in 20 µl 5% acetonitrile containing 0.1% (vol/vol) trifluoroacetic acid and separated on a NanoAcquity (Waters) UPLC. In brief, a 4.0-µl injection was loaded in 5% acetonitrile containing 0.1% formic acid at 4.0 µl/min for 4.0 min onto a 100-µm I.D. fused-silica precolumn packed with 2 cm of 5-µm (200 Å) Magic C18AQ (Bruker-Michrom) and eluted using a gradient at 300 nl/min onto a 75-µm I.D. analytical column packed with 25 cm of 3-µm (100 Å) Magic C18AQ particles to a gravity-pulled tip. The solvents were A, water (0.1% formic acid); and B, acetonitrile (0.1% formic acid). A linear gradient was developed from 5% solvent A to 35% solvent B in 60 min. Ions were introduced by positive electrospray ionization via liquid junction into a Q Exactive hybrid mass spectrometer (Thermo). Mass spectra were acquired over *m/z* 300–1750 at 70,000 resolution (*m/z* 200) and data-dependent acquisition selected the top 10 most abundant precursor ions for tandem mass spectrometry by high-energy collisional dissociation fragmentation using an isolation width of 1.6 Da, collision energy of 27, and a resolution of 17,500.

Data analysis. Raw data files were peak processed with Proteome Discoverer (version 1.4, Thermo) prior to database searching with Mascot Server (version 2.4) against the Chlamy Index of NCBInr database. Search parameters included trypsin specificity with two missed cleavages or no enzymatic specificity. The variable modifications of oxidized methionine, pyroglutamic acid for N-terminal glutamine, N-terminal acetylation of the protein, and a fixed modification for carbamidomethyl cysteine were considered. The mass tolerances were 10 ppm for the precursor and 0.05 Da for the fragments. Search results were then loaded into the Scaffold Viewer (Proteome Software) for peptide/protein validation and label-free quantitation.

To identify proteins specifically missing or greatly reduced in *fap44* axonemes, all the identified proteins were further filtered to select only proteins with confidence above 95%, with at least five peptides identified and with peptide confidence above 95%. This reduced the total to 625 proteins. These proteins were further filtered to those whose normalized abundances in the mutant were less than 0.2 that of the same proteins in wild type and whose abundances in wild-type axonemes were equal to or greater than ¼ that of FAP44 using Top 3 Precursor Intensity as a quantitative value (Silva *et al.*, 2006). These criteria reduced the list to 10 proteins, four of which are extracellular matrix proteins. The latter are common contaminants in flagellar preparations, and it is not unexpected that they would be greatly reduced in the *fap44* sample since the *fap44* mutant originated from a cell-wall–less strain.

Immunoprecipitation of purified FAP44, FAP43, and IDA *f*

Dyneins were extracted from the axonemes with 0.6 M NaCl in HMDE (HMDENa without NaCl) buffer. The extract was first clarified by centrifugation at 40,000 × *g* for 20 min, diluted fivefold with HMDE buffer, applied onto a UnoQ anion exchange column (Bio-Rad, Hercules, CA), and eluted with a linear gradient of 130–350 mM NaCl in HMDE buffer. Peak fractions containing IDA *f* were combined and diluted 2.5-fold (final ~100 mM NaCl) with HMDE buffer. Streptavidin-agarose (Sigma-Aldrich) preequilibrated with HMDE plus 100 mM NaCl was added to the IDA *f*-solution and incubated for 2 h at 4°C. The agarose beads were washed three times with HMDE plus 100 mM NaCl, and the bound proteins were released by boiling in the sample buffer. For a negative control, streptavidin-agarose was incubated with 1 mM biocytin (Sigma-Aldrich) for 1 h at 4°C before incubation with the IDA *f*-solution.

ACKNOWLEDGMENTS

This work was supported by the Kazato Research Foundation (to T.O.); the Takeda Science Foundation (to T.O. and T. K.); the Japan Society for the Promotion of Science KAKENHI grant numbers 15H01202, 17H05057 (to T.O.), and 17K15115 (to T.K.); the Naito Foundation (to T.O.); the Uehara Memorial Foundation (to T.O.); the Senri Life Science Foundation (to T.O.); the Institute for Fermentation, Osaka (to T.O.); the Ichiro Kanehara Foundation (to T.K.); National Institutes of Health grants R37 GM030626 and R35 GM122574 (to G.W.); and the Robert W. Booth Endowment at the University of Massachusetts Medical School (to G.W.). The structural analysis part of this research is partially supported by the Platform Project for Supporting Drug Discovery and Life Science Research (Basis for Supporting Innovative Drug Discovery and Life Science Research, BINDS) from the Japan Agency for Medical Research and Development, AMED. We thank Masahide Kikkawa and Haruaki Yanagisawa (University of Tokyo, Japan) for their invaluable advice and assistance in the operation of the electron microscope. We are grateful to John Leszyk and the University of Massachusetts Medical School's Mass Spectrometry Facility for expert assistance with the mass spectrometry.

REFERENCES

Adams GM, Huang B, Piperno G, Luck DJ (1981). Central-pair microtubular complex of *Chlamydomonas* flagella: polypeptide composition as revealed by analysis of mutants. J Cell Biol 91, 69–76.

Afzelius BA (2004). Cilia-related diseases. J Pathol 204, 470–477.

Bower R, VanderWaal K, O'Toole E, Fox L, Perrone C, Mueller J, Wirschell M, Kamiya R, Sale WS, Porter ME (2009). IC138 defines a subdomain at the base of the I1 dynein that regulates microtubule sliding and flagellar motility. Mol Biol Cell 20, 3055–3063.

Bui KH, Sakakibara H, Movassagh T, Oiwa K, Ishikawa T (2008). Molecular architecture of inner dynein arms in situ in *Chlamydomonas reinhardtii* flagella. J Cell Biol 183, 923–932.

Bui KH, Yagi T, Yamamoto R, Kamiya R, Ishikawa T (2012). Polarity and asymmetry in the arrangement of dynein and related structures in the *Chlamydomonas* axoneme. J Cell Biol 198, 913–925.

Carter AP, Garbarino JE, Wilson-Kubalek EM, Shipley WE, Cho C, Milligan RA, Vale RD, Gibbons IR (2008). Structure and functional role of dynein's microtubule-binding domain. Science 322, 1691–1695.

Cho C, Vale RD (2012). The mechanism of dynein motility: insight from crystal structures of the motor domain. Biochim Biophys Acta 1823, 182–191.

DiBella LM, Sakato M, Patel-King RS, Pazour GJ, King SM (2004a). The LC7 light chains of *Chlamydomonas* flagellar dyneins interact with

components required for both motor assembly and regulation. Mol Biol Cell 15, 4633–4646.
DiBella LM, Smith EF, Patel-King RS, Wakabayashi K, King SM (2004b). A novel Tctex2-related light chain is required for stability of inner dynein arm I1 and motor function in the *Chlamydomonas* flagellum. J Biol Chem 279, 21666–21676.
Elam CA, Sale WS, Wirschell M (2009). The regulation of dynein-driven microtubule sliding in *Chlamydomonas* flagella by axonemal kinases and phosphatases. Methods Cell Biol 92, 133–151.
Furuta A, Yagi T, Yanagisawa HA, Higuchi H, Kamiya R (2009). Systematic comparison of in vitro motile properties between *Chlamydomonas* wild-type and mutant outer arm dyneins each lacking one of the three heavy chains. J Biol Chem 284, 5927–5935.
Gaillard AR, Diener DR, Rosenbaum JL, Sale WS (2001). Flagellar radial spoke protein 3 is an A-kinase anchoring protein (AKAP). J Cell Biol 153, 443–448.
Gaillard AR, Fox LA, Rhea JM, Craige B, Sale WS (2006). Disruption of the A-kinase anchoring domain in flagellar radial spoke protein 3 results in unregulated axonemal cAMP-dependent protein kinase activity and abnormal flagellar motility. Mol Biol Cell 17, 2626–2635.
Gibbons BH, Gibbons IR (1987). Vanadate-sensitized cleavage of dynein heavy chains by 365-nm irradiation of demembranated sperm flagella and its effect on the flagellar motility. J Biol Chem 262, 8354–8359.
Gibbons IR (1981). Cilia and flagella of eukaryotes. J Cell Biol 91, 107s–124s.
Gokhale A, Wirschell M, Sale WS (2009). Regulation of dynein-driven microtubule sliding by the axonemal protein kinase CK1 in *Chlamydomonas* flagella. J Cell Biol 186, 817–824.
Goodenough UW, Heuser JE (1982). Substructure of the outer dynein arm. J Cell Biol 95, 798–815.
Goodstein DM, Shu S, Howson R, Neupane R, Hayes RD, Fazo J, Mitros T, Dirks W, Hellsten U, Putnam N, Rokhsar DS (2012). Phytozome: a comparative platform for green plant genomics. Nucleic Acids Res 40, D1178–D1186.
Habermacher G, Sale WS (1997). Regulation of flagellar dynein by phosphorylation of a 138-kD inner arm dynein intermediate chain. J Cell Biol 136, 167–176.
Harrison A, Olds-Clarke P, King SM (1998). Identification of the t complex-encoded cytoplasmic dynein light chain tctex1 in inner arm I1 supports the involvement of flagellar dyneins in meiotic drive. J Cell Biol 140, 1137–1147.
Hendrickson TW, Perrone CA, Griffin P, Wuichet K, Mueller J, Yang P, Porter ME, Sale WS (2004). IC138 is a WD-repeat dynein intermediate chain required for light chain assembly and regulation of flagellar bending. Mol Biol Cell 15, 5431–5442.
Heumann JM, Hoenger A, Mastronarde DN (2011). Clustering and variance maps for cryo-electron tomography using wedge-masked differences. J Struct Biol 175, 288–299.
Heuser T, Barber CF, Lin J, Krell J, Rebesco M, Porter ME, Nicastro D (2012). Cryoelectron tomography reveals doublet-specific structures and unique interactions in the I1 dynein. Proc Natl Acad Sci USA 109, E2067–E2076.
Hirokawa N, Tanaka Y, Okada Y, Takeda S (2006). Nodal flow and the generation of left-right asymmetry. Cell 125, 33–45.
Huang J, Roberts AJ, Leschziner AE, Reck-Peterson SL (2012). Lis1 acts as a "clutch" between the ATPase and microtubule-binding domains of the dynein motor. Cell 150, 975–986.
Ikeda K, Yamamoto R, Wirschell M, Yagi T, Bower R, Porter ME, Sale WS, Kamiya R (2009). A novel ankyrin-repeat protein interacts with the regulatory proteins of inner arm dynein f (I1) of *Chlamydomonas reinhardtii*. Cell Motil Cytoskeleton 66, 448–456.
Jones DT, Cozzetto D (2015). DISOPRED3: precise disordered region predictions with annotated protein-binding activity. Bioinformatics 31, 857–863.
Kagami O, Kamiya R (1992). Translocation and rotation of microtubules caused by multiple species of *Chlamydomonas* inner-arm dynein. J Cell Sci 103, 653–664.
Kamiya R (1988). Mutations at twelve independent loci result in absence of outer dynein arms in Chylamydomonas *reinhardtii*. J Cell Biol 107, 2253–2258.
Kamiya R, Kurimoto E, Muto E (1991). Two types of *Chlamydomonas* flagellar mutants missing different components of inner-arm dynein. J Cell Biol 112, 441–447.
Kamiya R, Okamoto M (1985). A mutant of *Chlamydomonas reinhardtii* that lacks the flagellar outer dynein arm but can swim. J Cell Sci 74, 181–191.
Kamiya R, Yagi T (2014). Functional diversity of axonemal dyneins as assessed by in vitro and in vivo motility assays of *Chlamydomonas* mutants. Zoolog Sci 31, 633–644.
Kato T, Kagami O, Yagi T, Kamiya R (1993). Isolation of two species of *Chlamydomonas reinhardtii* flagellar mutants, ida5 and ida6, that lack a newly identified heavy chain of the inner dynein arm. Cell Struct Funct 18, 371–377.
King SJ, Dutcher SK (1997). Phosphoregulation of an inner dynein arm complex in *Chlamydomonas reinhardtii* is altered in phototactic mutant strains. J Cell Biol 136, 177–191.
King SM (2000). The dynein microtubule motor. Biochim Biophys Acta 1496, 60–75.
Kon T, Nishiura M, Ohkura R, Toyoshima YY, Sutoh K (2004). Distinct functions of nucleotide-binding/hydrolysis sites in the four AAA modules of cytoplasmic dynein. Biochemistry 43, 11266–11274.
Kon T, Oyama T, Shimo-Kon R, Imamula K, Shima T, Sutoh K, Kurisu G (2012). The 2.8 A crystal structure of the dynein motor domain. Nature 484, 345–350.
Kotani N, Sakakibara H, Burgess SA, Kojima H, Oiwa K (2007). Mechanical properties of inner-arm dynein-f (dynein I1) studied with in vitro motility assays. Biophys J 93, 886–894.
Koutoulis A, Pazour GJ, Wilkerson CG, Inaba K, Sheng H, Takada S, Witman GB (1997). The *Chlamydomonas reinhardtii* ODA3 gene encodes a protein of the outer dynein arm docking complex. J Cell Biol 137, 1069–1080.
Kremer JR, Mastronarde DN, McIntosh JR (1996). Computer visualization of three-dimensional image data using IMOD. J Struct Biol 116, 71–76.
Kubo T, Hirono M, Aikawa T, Kamiya R, Witman GB (2015). Reduced tubulin polyglutamylation suppresses flagellar shortness in Chlamydomonas. Mol Biol Cell 26, 2810–2822.
LeDizet M, Piperno G (1995). The light chain p28 associates with a subset of inner dynein arm heavy chains in *Chlamydomonas* axonemes. Mol Biol Cell 6, 697–711.
Li X, Zhang R, Patena W, Gang SS, Blum SR, Ivanova N, Yue R, Robertson JM, Lefebvre PA, Fitz-Gibbon ST, *et al*. (2016). An indexed, mapped mutant library enables reverse genetics studies of biological processes in *Chlamydomonas reinhardtii*. Plant Cell 28, 367–387.
Lin H, Zhang Z, Guo S, Chen F, Kessler JM, Wang YM, Dutcher SK (2015). A NIMA-related kinase suppresses the flagellar instability associated with the loss of multiple axonemal structures. PLoS Genet 11, e1005508.
Lin J, Okada K, Raytchev M, Smith MC, Nicastro D (2014). Structural mechanism of the dynein power stroke. Nat Cell Biol 16, 479–485.
Lin J, Yin W, Smith MC, Song K, Leigh MW, Zariwala MA, Knowles MR, Ostrowski LE, Nicastro D (2014). Cryo-electron tomography reveals ciliary defects underlying human RSPH1 primary ciliary dyskinesia. Nat Commun 5, 5727.
Mastronarde DN (2005). Automated electron microscope tomography using robust prediction of specimen movements. J Struct Biol 152, 36–51.
McKenney RJ, Vershinin M, Kunwar A, Vallee RB, Gross SP (2010). LIS1 and NudE induce a persistent dynein force-producing state. Cell 141, 304–314.
Metlagel Z, Kikkawa YS, Kikkawa M (2007). Ruby-Helix: an implementation of helical image processing based on object-oriented scripting language. J Struct Biol 157, 95–105.
Mitchell DR, Rosenbaum JL (1985). A motile *Chlamydomonas* flagellar mutant that lacks outer dynein arms. J Cell Biol 100, 1228–1234.
Movassagh T, Bui KH, Sakakibara H, Oiwa K, Ishikawa T (2010). Nucleotide-induced global conformational changes of flagellar dynein arms revealed by in situ analysis. Nat Struct Mol Biol 17, 761–767.
Myster SH, Knott JA, O'Toole E, Porter ME (1997). The *Chlamydomonas* Dhc1 gene encodes a dynein heavy chain subunit required for assembly of the I1 inner arm complex. Mol Biol Cell 8, 607–620.
Myster SH, Knott JA, Wysocki KM, O'Toole E, Porter ME (1999). Domains in the 1alpha dynein heavy chain required for inner arm assembly and flagellar motility in *Chlamydomonas*. J Cell Biol 146, 801–818.
Nicastro D, Schwartz C, Pierson J, Gaudette R, Porter ME, McIntosh JR (2006). The molecular architecture of axonemes revealed by cryoelectron tomography. Science 313, 944–948.
Oda T (2017). Three-dimensional structural labeling microscopy of cilia and flagella. Microscopy (Oxf) 66, 234–244.
Oda T, Kikkawa M (2013). Novel structural labeling method using cryo-electron tomography and biotin-streptavidin system. J Struct Biol 183, 305–311.
Oda T, Yanagisawa H, Kamiya R, Kikkawa M (2014). A molecular ruler determines the repeat length in eukaryotic cilia and flagella. Science 346, 857–860.
Oda T, Yanagisawa H, Kikkawa M (2015). Detailed structural and biochemical characterization of the nexin-dynein regulatory complex. Mol Biol Cell 26, 294–304.

Oda T, Yanagisawa H, Yagi T, Kikkawa M (2014). Mechanosignaling between central apparatus and radial spokes controls axonemal dynein activity. J Cell Biol 204, 807–819.
Okita N, Isogai N, Hirono M, Kamiya R, Yoshimura K (2005). Phototactic activity in *Chlamydomonas* 'non-phototactic' mutants deficient in Ca2+-dependent control of flagellar dominance or in inner-arm dynein. J Cell Sci 118, 529–537.
Pazour GJ, Agrin N, Leszyk J, Witman GB (2005). Proteomic analysis of a eukaryotic cilium. J Cell Biol 170, 103–113.
Pazour GJ, Rosenbaum JL (2002). Intraflagellar transport and cilia-dependent diseases. Trends Cell Biol 12, 551–555.
Perrone CA, Myster SH, Bower R, O'Toole ET, Porter ME (2000). Insights into the structural organization of the I1 inner arm dynein from a domain analysis of the 1beta dynein heavy chain. Mol Biol Cell 11, 2297–2313.
Perrone CA, Yang P, O'Toole E, Sale WS, Porter ME (1998). The *Chlamydomonas* IDA7 locus encodes a 140-kDa dynein intermediate chain required to assemble the I1 inner arm complex. Mol Biol Cell 9, 3351–3365.
Pettersen EF, Goddard TD, Huang CC, Couch GS, Greenblatt DM, Meng EC, Ferrin TE (2004). UCSF Chimera—a visualization system for exploratory research and analysis. J Comput Chem 25, 1605–1612.
Pigino G, Bui KH, Maheshwari A, Lupetti P, Diener D, Ishikawa T (2011). Cryoelectron tomography of radial spokes in cilia and flagella. J Cell Biol 195, 673–687.
Pigino G, Maheshwari A, Bui KH, Shingyoji C, Kamimura S, Ishikawa T (2012). Comparative structural analysis of eukaryotic flagella and cilia from *Chlamydomonas*, Tetrahymena, and sea urchins. J Struct Biol 178, 199–206.
Piperno G, Huang B, Luck DJ (1977). Two-dimensional analysis of flagellar proteins from wild-type and paralyzed mutants of *Chlamydomonas reinhardtii*. Proc Natl Acad Sci USA 74, 1600–1604.
Piperno G, Ramanis Z, Smith EF, Sale WS (1990). Three distinct inner dynein arms in *Chlamydomonas* flagella: molecular composition and location in the axoneme. J Cell Biol 110, 379–389.
Porter ME, Power J, Dutcher SK (1992). Extragenic suppressors of paralyzed flagellar mutations in *Chlamydomonas reinhardtii* identify loci that alter the inner dynein arms. J Cell Biol 118, 1163–1176.
Rompolas P, Patel-King RS, King SM (2012). Association of Lis1 with outer arm dynein is modulated in response to alterations in flagellar motility. Mol Biol Cell 23, 3554–3565.
Sanders MA, Salisbury JL (1995). Immunofluorescence microscopy of cilia and flagella. Methods Cell Biol 47, 163–169.
Satir P, Christensen ST (2007). Overview of structure and function of mammalian cilia. Annu Rev Physiol 69, 377–400.
Schmidt H, Gleave ES, Carter AP (2012). Insights into dynein motor domain function from a 3.3-A crystal structure. Nat Struct Mol Biol 19, 492–497, S1.
Silva JC, Gorenstein MV, Li GZ, Vissers JP, Geromanos SJ (2006). Absolute quantification of proteins by LCMSE: a virtue of parallel MS acquisition. Mol Cell Proteomics 5, 144–156.
Smith EF, Sale WS (1991). Microtubule binding and translocation by inner dynein arm subtype I1. CellMotil Cytoskeleton 18, 258–268.
Taillon BE, Jarvik JW (1995). Release of the cytoskeleton and flagellar apparatus from *Chlamydomonas*. Methods Cell Biol 47, 307–313.
Tanaka AS, Tanaka M (2017). A novel gene, cilia flagella associated protein 44, encoding an enzyme cleaving FtsZ and tubulin contributes to the regulation of secretory pathway. Biochem Biophys Res Commun 493, 399–408.
Tang S, Wang X, Li W, Yang X, Li Z, Liu W, Li C, Zhu Z, Wang L, Wang J, *et al*. (2017). Biallelic mutations in CFAP43 and CFAP44 cause male infertility with multiple morphological abnormalities of the sperm flagella. Am J Hum Genet 100, 854–864.
Toba S, Fox LA, Sakakibara H, Porter ME, Oiwa K, Sale WS (2011). Distinct roles of 1alpha and 1beta heavy chains of the inner arm dynein I1 of *Chlamydomonas* flagella. Mol Biol Cell 22, 342–353.
Toropova K, Zou S, Roberts AJ, Redwine WB, Goodman BS, Reck-Peterson SL, Leschziner AE (2014). Lis1 regulates dynein by sterically blocking its mechanochemical cycle. Elife 3, e03372.
Ueno H, Bui KH, Ishikawa T, Imai Y, Yamaguchi T, Ishikawa T (2014). Structure of dimeric axonemal dynein in cilia suggests an alternative mechanism of force generation. Cytoskeleton (Hoboken) 71, 412–422.
Ueno H, Yasunaga T, Shingyoji C, Hirose K (2008). Dynein pulls microtubules without rotating its stalk. Proc Natl Acad Sci USA 105, 19702–19707.
VanderWaal KE, Yamamoto R, Wakabayashi K, Fox L, Kamiya R, Dutcher SK, Bayly PV, Sale WS, Porter ME (2011). bop5 Mutations reveal new roles for the IC138 phosphoprotein in the regulation of flagellar motility and asymmetric waveforms. Mol Biol Cell 22, 2862–2874.
Wakabayashi K, King SM (2006). Modulation of *Chlamydomonas reinhardtii* flagellar motility by redox poise. J Cell Biol 173, 743–754.
Wirschell M, Hendrickson T, Sale WS (2007). Keeping an eye on I1: I1 dynein as a model for flagellar dynein assembly and regulation. Cell Motil Cytoskeleton 64, 569–579.
Wirschell M, Yang C, Yang P, Fox L, Yanagisawa HA, Kamiya R, Witman GB, Porter ME, Sale WS (2009). IC97 is a novel intermediate chain of I1 dynein that interacts with tubulin and regulates interdoublet sliding. Mol Biol Cell 20, 3044–3054.
Witman GB, Carlson K, Berliner J, Rosenbaum JL (1972). *Chlamydomonas* flagella. I. Isolation and electrophoretic analysis of microtubules, matrix, membranes, and mastigonemes. J Cell Biol 54, 507–539.
Yagi T, Minoura I, Fujiwara A, Saito R, Yasunaga T, Hirono M, Kamiya R (2005). An axonemal dynein particularly important for flagellar movement at high viscosity. Implications from a new *Chlamydomonas* mutant deficient in the dynein heavy chain gene DHC9. J Biol Chem 280, 41412–41420.
Yamamoto R, Obbineni JM, Alford LM, Ide T, Owa M, Hwang J, Kon T, Inaba K, James N, King SM, *et al*. (2017). Chlamydomonas DYX1C1/PF23 is essential for axonemal assembly and proper morphology of inner dynein arms. PLoS Genet 13, e1006996.
Yamamoto R, Song K, Yanagisawa HA, Fox L, Yagi T, Wirschell M, Hirono M, Kamiya R, Nicastro D, Sale WS (2013). The MIA complex is a conserved and novel dynein regulator essential for normal ciliary motility. J Cell Biol 201, 263–278.
Yang P, Fox L, Colbran RJ, Sale WS (2000). Protein phosphatases PP1 and PP2A are located in distinct positions in the *Chlamydomonas* flagellar axoneme. J Cell Sci 113, 91–102.